CHAPTER V

Role of TiO_2 as a core and shell in two different core-shell nanocomposites for photocatalytic degradation of MB dye

In the earlier chapters, we have discussed in details about core-shell TiO_2-MgO and TiO_2-SnO_2 nanostructures. We coated the material TiO_2 with two different layers. The first layer tried was MgO which has an insulating band gap of 7.8 eV. The other layer was SnO_2 whose band gap is 3.37 eV which is very close to that of TiO_2 itself. In this chapter we will discuss about two other core-shell nanocomposite structures where for one, the shell is ZrO_2 with a band gap 5.7 eV and for the other, TiO_2 will act as a shell material with a core nanostructure of CdSe which has a very small band gap 1.74 eV. Also another interesting fact that has come to notice. Whilst in our earlier chapters, we have studied materials which have TYPE 2 band edge at their bulk structure, now both TiO_2-ZrO_2 and CdSe-TiO_2 have bulk band edge as TYPE 1. So, in this chapter, we shall addess the following questions:

- ✓ Can a material with a TYPE 1 band alignment in the bulk form be converted to TYPE 2 when it comes down to nanosize? Can these be rendered as efficient photocatalyst?
- ✓ As a shell material, what is the role of TiO_2 as a shell layer for supporting photocatalysis?

So, with an aim to answer the above questions we have focused on the optical and photocatalytic properties of TiO_2-ZrO_2 and CdSe-TiO_2 core-shell nanocomposites. The optical and structural details are characterized via UV-vis absorbance spectra, PL spectra, XRD, RAMAN and TEM. The photocatalytic activity for both the samples are studied for degradation of Methylene Blue (MB) dye under daylight illumination for different time limits.

5.1 Synthesis of core-shell TiO_2-ZrO_2 nanostructures

The TiO_2 nanoparticles were synthesized as we have described in chapter 3. For preparation of ZrO_2 coating layer, we followed a standard procedure [1]. 2.312 g of $ZrO(NO_3)_2 \cdot xH_2O$ and 4 g of NaOH were dissolved, each in 20 ml of distilled water, to form 0.5 M and 5 M solutions, respectively. The NaOH solution was slowly added to the $ZrO(NO_3)_2 \cdot xH_2O$ solution and stirred for ~4 hour. Then the resultant solution was poured dropwise on the already prepared TiO_2 nanoparticles under stirring which continued for 8 hours. Then the solution was centrifuged and dried at 100° C to remove

the water from the sample so that there can be a coating of ZrO_2 over the TiO_2 nanoparticles.

5.2 Structural characterization

5.2.1 XRD pattern analysis

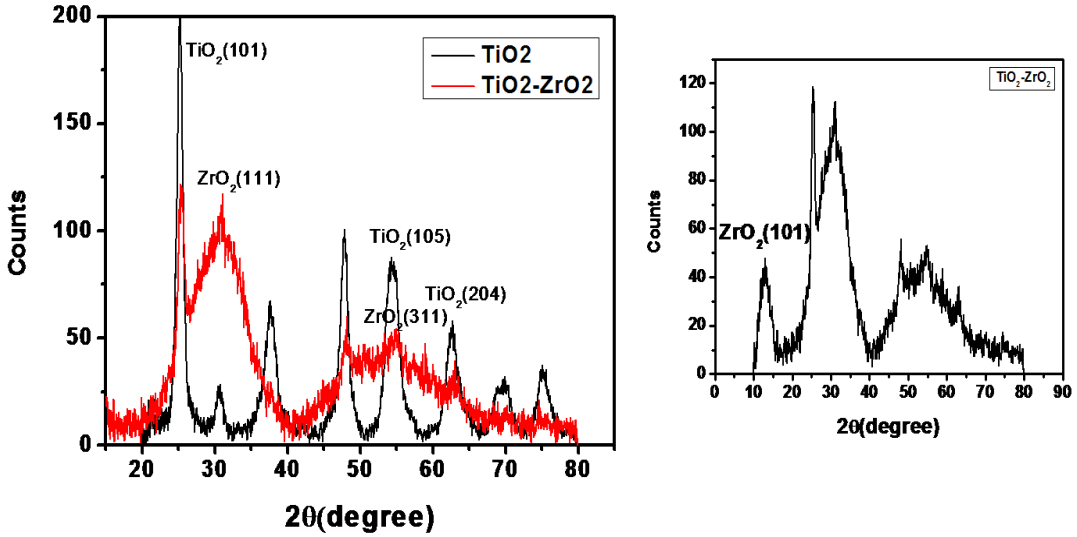

Fig 5.1: (left) XRD pattern of TiO_2 nanoparticles and core-shell TiO_2-ZrO_2 nanostructures and (right) extended version of XRD of TiO_2-ZrO_2 nanostructures

Fig 5.1 shows the XRD patterns of core TiO_2 and core-shell TiO_2-ZrO_2 nanostructures. We can see that the core–shell nanostructure (red line) consists of both core TiO_2 and shell ZrO_2 phases. It contains anatase phase of core TiO_2 and monoclinic phase of shell ZrO_2. The figure in the right hand side shows an extended version of the core-shell nanostructure where we can see the prime peak of ZrO_2 (101). The crystallite size and microstrain are calculated as described in chapter 2 (section 2.2.1) from W-H equation.

Table 5.1: Calculation of crystallite size and microstrain

Sample name	Crystallite size (nm)	Microstrain
TiO_2	8.5	0.006
TiO_2-ZrO_2	4.4	-0.011

From the table 5.1, it can be seen that the crystallite size is less in the core-shell nanocomposite than that of the core structure. This is a different observation as we found in TiO_2-MgO and TiO_2-SnO_2 the coating layer favored increase in crystallite size by extending the crystallinity of the sample. Also the microstrain as obtained in the core-shell nanostructure is negative. Again from the XRD pattern, it is clear that as the shell is grown, the diffraction peaks shift toward smaller *d*-spacing (larger 2θ). This provides a clear indication that the growth of the ZrO_2 shell is compressing the lattice planes in the TiO_2 core. Compressive strain is generally defined as the deformation along a line segment that decreases in length when a load is applied. The decrease in crystallite size of the core-shell hints towards a strong dependence of crystallite size upon the induced strain by shell [2]. The results indicate that tensile strain exists in pure TiO_2 nanocrystals, whereas compressive strain is obtained after surface coating leading to smaller crystallite size. Also compressive force often results in a negative strain as we have observed in the core-shell structure. Therefore, in a nutshell, it can be marked that the surface coating plays an important role in tuning the crystallite size and lattice strain of core-shell nanostructure [2].

5.2.2 TEM image analysis

The low resolution TEM image shows that the particles have sizes carrying from 5 nm - 20 nm. But the core-shell morphology is not clear in the low resolution image. From the HRTEM image, the evidence of formation of core-shell is found as we can see two different types of lattice lanes which correspond to two different materials. The red colored planes are assigned to core TiO_2 and the yellow colored planes are drawn for the shell ZrO_2 (Fig. 5.2, left).

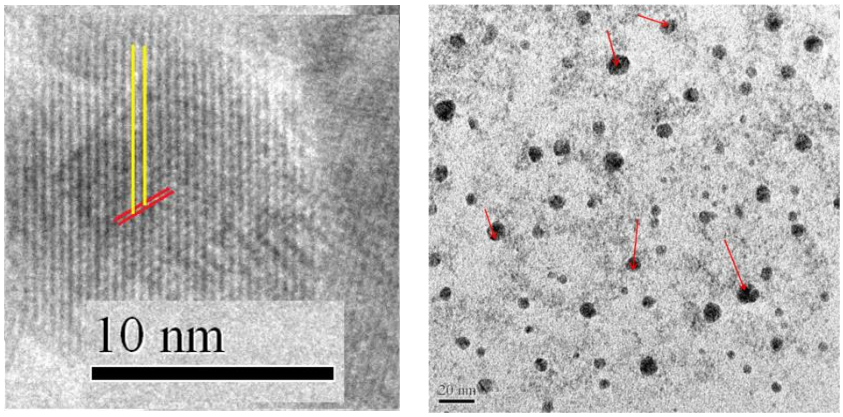

Fig 5.2: (left) HRTEM image (right) Low resolution TEM image of core-shell TiO_2-ZrO_2 nanocomposites

5.2.3 EDX spectra analysis

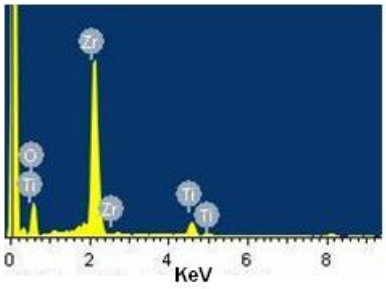

Fig 5.3: EDX spectra of TiO_2-ZrO_2 nanoparticles

The EDX spectrum confirms the presence of all the constituent elements Ti, Zr and O in the sample.

5.2.4 Raman Spectra analysis

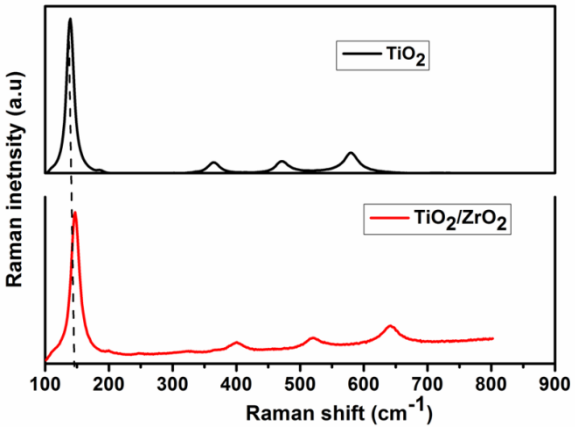

Fig 5.4: Raman spectra of TiO_2 and core-shell TiO_2-ZrO_2 nanostructure

Fig 5.4 displays the Raman spectra of core TiO_2 and core-shell TiO_2-ZrO_2 nanoscomposites. As we have already mentioned in the earlier chapter 3 (section 3.6.5), anatase TiO_2 has six Raman active modes and three infrared (IR) active modes. The optical phonon mode at the Γ-point of Brillouin zone (BZ) is presented by [3-4].

$$\Gamma = A1g(R) + 2B1g(R) + 3Eg(R) + B2u(IR) + A2u(IR) + 2Eu(IR) \quad \ldots\ldots\ldots (5.1)$$

The four vibrations (A1g+B1g+B2g+Eg) are Raman active and the rest are IR active. In the pristine TiO_2 sample, the intense Eg peak has appeared at 144 cm^{-1}, followed by low intense A1g, B1g peaks at 410 cm^{-1}, 520 cm^{-1} and at 630 cm^{-1} respectively [5-6]. But in case of core-shell TiO_2-ZrO_2 nanostructures, as we can see from figure, the Eg peak is blue shifted to 148 cm^{-1} unlike the other core-shells we have discussed in chapter 3. The other three peaks are also found to be blue shifted than their corresponding core positions. The intensity of the Raman peaks are suppressed in the core-shell structure than the core structure.

Surface atoms of nanoparticles are attached together by weaker forces because of absent neighbors, which leads to lower characteristic wavenumbers for these atoms compared with interior atoms. When the surface of TiO_2 is coated with a layer of ZrO_2, an alteration occurs and the surface atoms get bound differently. Furthermore, the coating layer produces a compressive stress on the first several layer atoms of TiO_2 nanoparticles which we already proved from the XRD pattern. This makes the surface atoms to pack intimately, resulting in higher vibrational wavenumbers [7]. The decrease in Raman peak suggests that the core is completely covered with the shell layer thus obstructing the phonons to interact with the outer phonons.

Xu et al. [7] used a phonon confinement model to explain the observed changes in the Raman line and position using Heisenberg uncertainty principle.

$$\Delta X \times \Delta P \geq \frac{h}{2} \ldots\ldots\ldots\ldots\ldots\ldots (5.2)$$

Where ΔX is crystallite size, ΔP is the phonon momentum distribution and h is Planck constant. In case of a perfect crystal first order Raman scattering of photons obey the phonon selection rule k=0, implying phonon contribution at the center of Brillouin zone. Thus when ΔX decreases as we can see in our case, Δp increases thus

the phonon contribution becomes very less. This results in shifting as well as expansion of the active Raman peak.

Thus as we have already explained the Raman active peak width is increased in the core-shell structure whilst the phonon lifetime is decreased. This is due to the fact that as the crystallite size becomes smaller, the phonon density decreases and also anharmonic phonon coupling decreases. Also with decrease in crystallite size, since the phonon momentum distribution increases, some of the phonons may get lost in collision with each other thus shortening its life span.

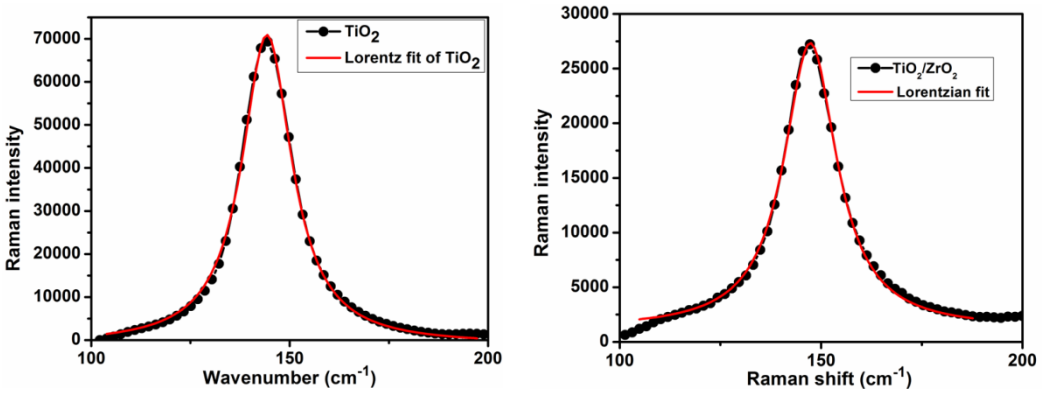

Fig 5.5: Lorentzian fit on Raman active mode of (left) TiO_2 and (right) TiO_2-ZrO_2

Table 5.2: Calculation of bond width of Raman active peak and phonon lifetime

Sample name	Eg bond width (cm^{-1})	Phonon lifetime (ps)
TiO_2	15.29	0.32
TiO_2-ZrO_2	15.99	0.31

5.3 Optical Property analysis

5.3.1 UV-vis absorbance spectra analysis

Fig 5.6 shows the UV-vis absorbance spectra of core TiO_2 and core-shell TiO_2-ZrO_2 nanocomposite. It is seen that absorbance maxima of TiO_2 which occurred at ~350 nm is shifted to 355 nm after coating with ZrO_2. This slight red shift occurs due to increase in particle size in the core-shell nanostructures. The absorption tail of TiO_2 in the visible region may be due to Ti^{3+} defect related states as well as oxygen vacancies

present in the sample which goes for the core-shell structure also as we have already observed in the other core-shell structures.

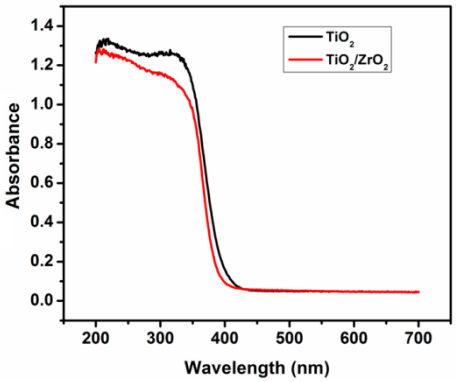

Fig 5.6: UV-vis absorbance spectra

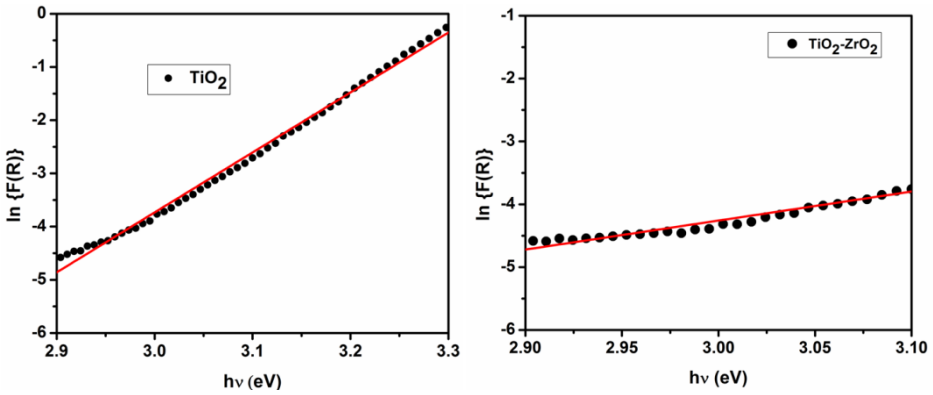

Fig 5.7: Urbach energy plot for (left) TiO_2 and (right) TiO_2-ZrO_2 nanostructures

The Urbach equation is represented by

$$\alpha = \alpha_0 \exp(E/E_\mu) \quad \text{.....(5.3)}$$

where α is the absorption coefficient, E is the photon energy and E_μ is the Urbach energy. For the calculation of Urbach energy, $ln\alpha$ is plotted against E. The reciprocal of the slopes of linear portion, below optical band gap, gives the same. In case of solid materials instead of α, $F(R)$ can also be plot which is calculated from the reflectance.

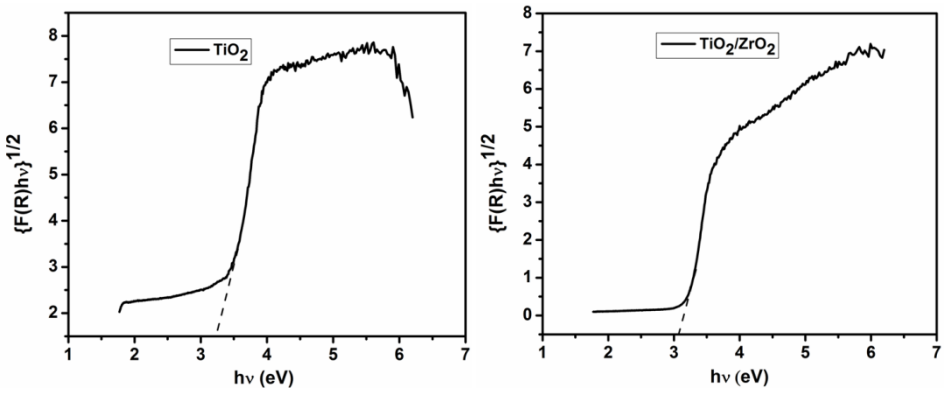

Fig 5.8 : Kubelka Munk Plot for (left) TiO_2 and (right) TiO_2-ZrO_2

The absorption is calculated by Kubelka-Munk plot $F(R) = (1-R)^2/2R$, where R is the reflectance of the sample and it is found from the reflectance spectra. The band gap of the nanomaterials were calculated from a plot of the modified Kubelka-Munk function $[F(R)\times E]^{1/2}$ vs the energy of absorbed light (E =hν) where $R = R_{sample} / R_{BaSO_4}$. After plotting the graphs and fitting linear, we get the band gaps as tabulated below.

Table 5.3: Calculation of band gap and Urbach energy

Sample name	Urbach energy (meV)	Band gap (eV)
TiO_2	90	3.3
TiO_2-ZrO_2	250	3.1

From the table 5.3 we can see that there is tremendous increase in Urbach energy when TiO_2 nanoparticles are coated with ZrO_2 shell layer. The growth of the shell generates strain and of defect states are created at the core/shell interface or within the shell as we stated in earlier chapters. These can act as trap states for photogenerated charge carriers. The excited electrons are captured by the shallow defect bands, preventing their direct transition to the conduction band as a result increasing the Urbach energy to such high extent. The band gap of the core-shell structure (3.1 eV) is also found to be less than that of the core structure (3.3 eV) which hints towards the TYPE 2 configuration of the system. The charge separation in the core-shell structure is schematically shown in Fig. 5.9.

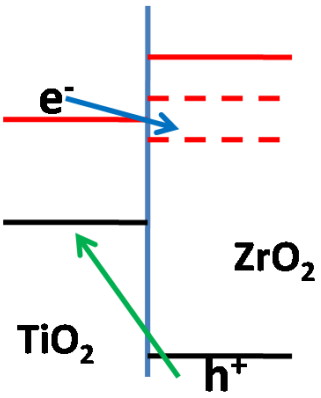

Fig 5.9: Schematic charge separation in TiO_2-ZrO_2

The red lines correspond to conduction band whilst the black ones represents the valence band. We can see that in bulk heterostructure, TiO_2-ZrO_2 possesses a TYPE 1 structure. But as the size decreases to nano regime, due to high surface to volume ratio lots of defect related states occur at the shell layer or at the core-shell interface. Thus as we have explained with increase in Urbach energy of the core-shell nanostructure, these shallow bands trap electrons preventing them from recombination. Thus a quasi TYPE 2 structure prevails in the TiO_2-ZrO_2 core-shell structure which is further confirmed from PL spectra.

5.3.2 Photoluminescence (PL) spectra analysis

Fig 5.10 shows the comparative PL spectra of core TiO_2 and core-shell TiO_2-ZrO_2 nanocomposites. It can be clearly seen from the figure that the intensity of the band edge emission peak is suppressed in the core-shell structure. If we look at the PL spectra, we can see that both core and the core-shell exhibit an emission peak at ~380 nm. This peak is assigned to phonon assisted indirect transition from $M \rightarrow \Gamma$ in the Brillouin zone as mentioned in chapter 3 (section 3.9.2) . The lowering of the peak is due to the coating layer of ZrO_2 surrounding TiO_2 as it does not allow sufficient amount of UV photons to go in and interact with the inner TiO_2 core thus reducing the PL intensity. Both samples exhibit an intense emission peak ~425 nm which is attributed to self trapped exciton (STE) recombination [8-9]. The other peaks correspond to defect related states or oxygen vacancy related states. Thus the PL

spectra also supports the quasi TYPE 2 structure in the core-shell structure which was earlier assumed from the band gap calculation.

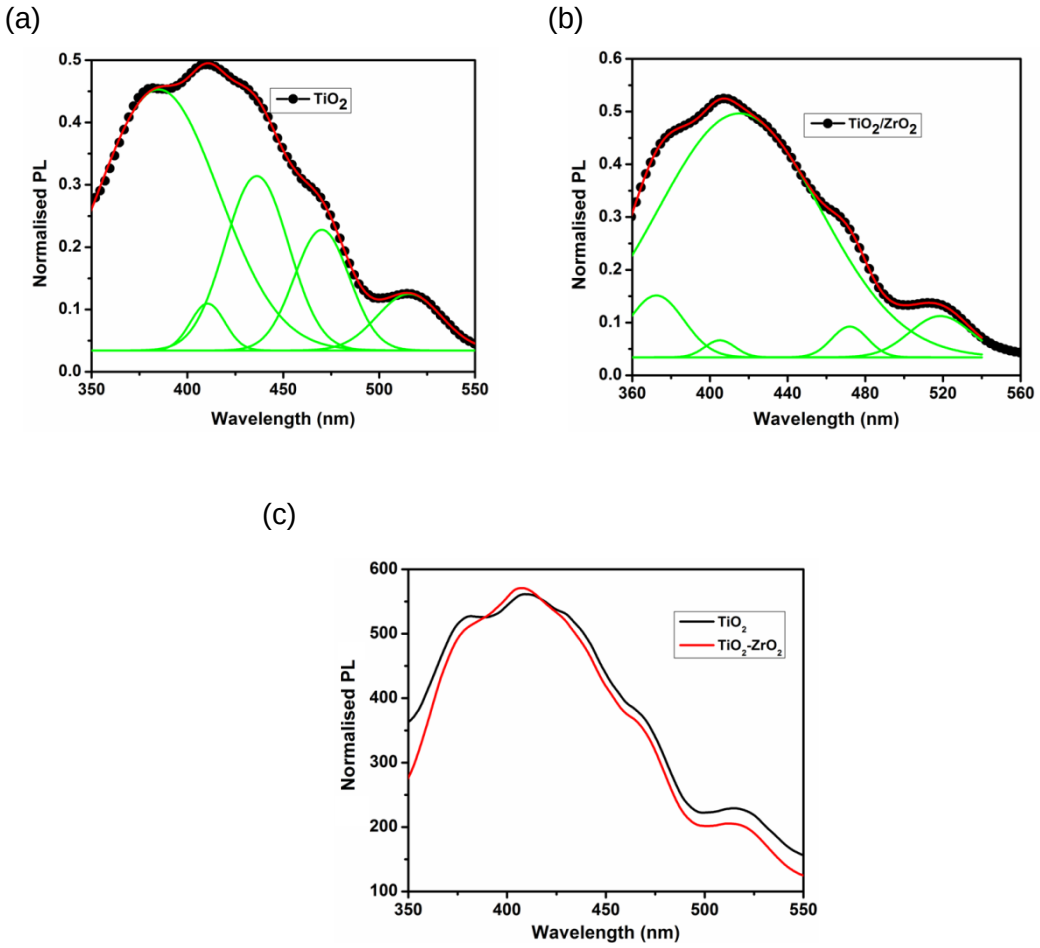

Fig 5.10: PL spectra of (a) core TiO_2, (b) TiO_2-ZrO_2 core-shell nanostructure and (c) comparative plot of both core and core-shell nanocomposites

5.3.3 Photocatalytic activity

Photocatalytic activities of pure TiO_2 nanoparticles and core-shell TiO_2-ZrO_2 nanoparticles are examined by observing the degradation of methylene blue (MB) under daylight. The photoactivity is observed under daylight lamp of 500 watt power Xenon lamp in the wavelength range from 400-700 nm. The samples are placed at 6 cm distance from the light in the photocatalysis chamber. For carrying out the degradation experiment, we followed the same procedure as stated in chapter 2 (section 2.3.3) . The catalyst loaded dye solution is irradiated under daylight different time limits. When irradiation is completed, each of the irradiated solution is

centrifuged at 13,000 rpm to make it free from the catalyst. 5 mL of each of the irradiated MB solution is taken for absorption measurement. The decrease of concentration or degradation of MB from its initial concentration is studied by observing the decrease of the absorption peak (C_t) of the dye solution irradiated for the aforementioned period. The degradation efficiency of phenol solution is given by$\{(C_0-C_t)/C_0\}\times100\%$ [10] where C_0 is the initial concentration of the dye solution. The rate constants are determined using 1st order kinetic equation.

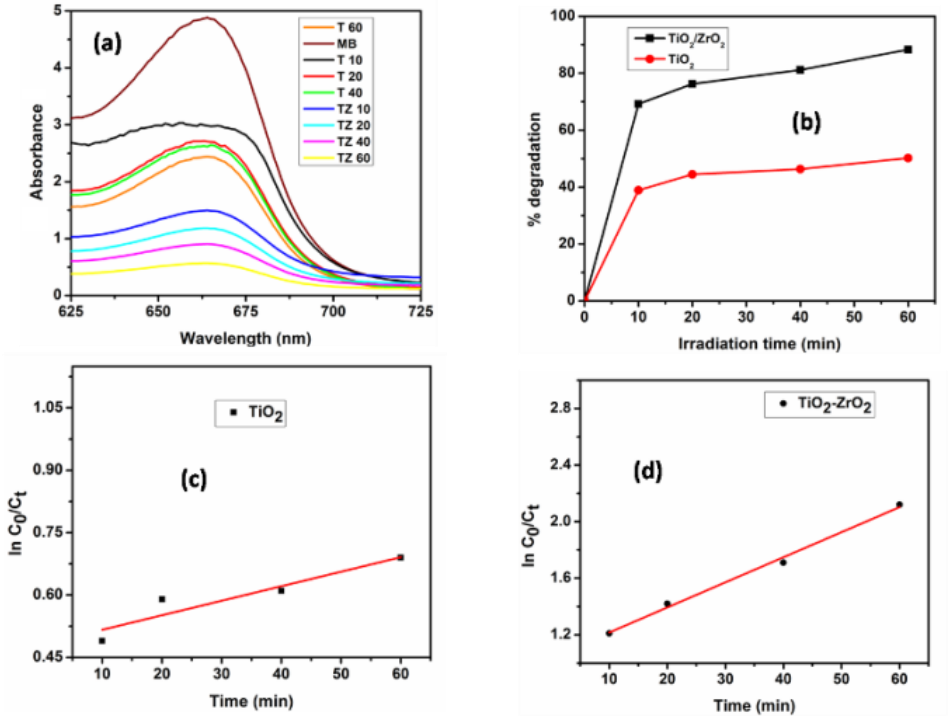

Fig 5.11: (a) Absorbance of methylene blue in presence of catalyst (b) % degradation, rate constant determination of (c) TiO_2 and (d) TiO_2-ZrO_2

Fig. 5.11 shows the photocatalytic degradation of MB in presence of TiO_2 as well as TiO_2-ZrO_2. The rate constants and percentage degradation amounts are tabulated below.

Table 5.4: Calculation of rate constant and % degradation

Sample name	Rate const (min^{-1})	% degradation w.r.t time			
		10 min	20 min	40 min	60 min
TiO_2	0.0035	38.9	44.47	46.31	50.2
TiO_2/ZrO_2	0.017	69.2	76.23	81.14	88.32

The table 5.4 clearly indicates that core-shell TiO_2-ZrO_2 nanostructures exhibit highest photocatalytic activity at 60 min irradiation which gradually increases from 10 min. The degradation efficiency is quite high if we compare it with the degradation shown by TiO_2 nanoparticles which is at maximum 50.2% at 60 min irradiation. The reaction mechanism for photocatalysis is same as we described in the earlier chapters. MB excited in the presence of sunlight can efficiently inject electrons into the TiO_2 conduction band. The slow degradation of MB by TiO_2 is due to electron recombination between the injected electron and surface adsorbed MB (holes). For the TiO_2-ZrO_2 core-shell system, electrons injected into the TiO_2 conduction band can be transferred to the different defect levels of ZrO_2 and then to the valence band. This leads to sufficient separation between the electron and hole. The electron in the defect states of ZrO_2 can then be trapped by dissolved oxygen to form reactive oxygen species which then degrade the dye MB. Again MB adsorbed directly onto the conduction band of ZrO_2 nanoparticles can inject electrons into the valence band of ZrO_2, which in turn leads to the degradation of MB via the same process described above. The rate constant calculated for both the samples also gives verdict in favor of the core-shell structure as a far better photocatalytic agent.

5.4 Synthesis of core-shell CdSe-TiO_2 nanocomposites

In a typical procedure[11], 0.4567 g (2 mmol) $CdCl_2 \cdot 2.5H_2O$ was dissolved in 100 mL of deionized water in a 250 mL three-neck flask, and 0.5 mL thioglycolic acid (TGA) was added while stirring. The solution was adjusted to pH 11.0 with 1.0 $mol \cdot L^{-1}$ NaOH solution. After several minutes, excess $NaBH_4$ (0.1 g) and 0.111 g (1 mmol) SeO_2 was added consecutively into the above solution**.** For the coating layer of TiO_2 nanoparticles, we followed a standard procedure. Titanium isopropoxide was taken as the reactant and 2-Propanol as the solvent in a ratio 2:5.Then we allowed the solution to stir for 30 minutes followed by adding few drops of H_2O and left it for stirring upto 8 hours until gel formation occurs. Then the solution is added dropwise to the already prepared CdSe solution to obtain the core-shell structure. The solution is centrifuged and dried at 100° C to get the powder core-shell structure.

5.5 Structural characterization

5.5.1 XRD pattern analysis

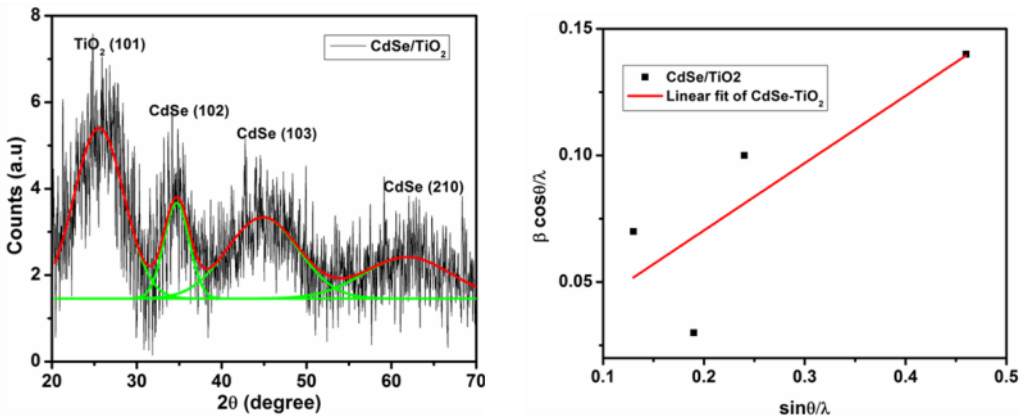

Fig 5.12: (left) XRD pattern (right) W-H Plot of CdSe-TiO_2

From the XRD, it can be seen that the peaks are quite broad indicating very small size in the core-shell structure. The peaks correspond to hexagonal CdSe structure along with tetragonal TiO_2 peak at $2\theta = 25.5^0$. We have determined the lattice strain and crystallite size of each sample using Williamson-Hall (*W-H*) equation

$$\beta\cos\theta/\lambda = 0.9/D + 4\epsilon\sin\theta/\lambda \quad \text{.....(5.4)}$$

In eqn. 5.4, λ is the wavelength of X-ray, β and θ are the FWHM and diffraction angle of the diffraction peaks of CdSe-TiO_2 core-shell nanocomposites. *D* is the effective crystallite size considering lattice strain and is the effective value of lattice strain. The crystallite size is found to be ~8 nm and lattice microstrain is obtained as 0.066.

5.5.2 TEM image analysis

Fig 5.13 (left) shows the low resolution TEM image of core-shell CdSe-TiO_2 nanocomposites . The shell contains two core nanoparticles which are indicated with blue colored arrows . The core particle size is about 7 nm and approximate diameter of the core-shell nanostructure is about 25 nm.The lattice planes of the core particle is illustrated with yellow color (right) while the same for shell layer is marked with red color. The interplanar spacing for the core and shell are obtained as 3 Å and 6 Å respectively.

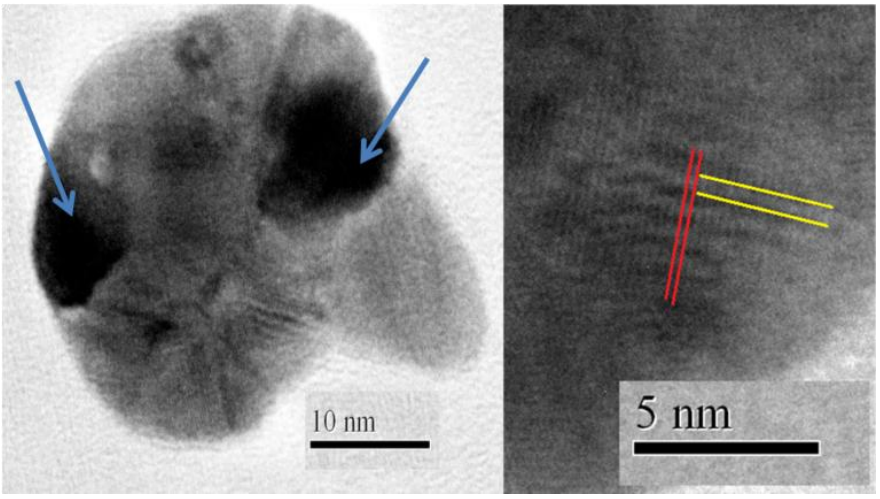

Fig 5.13: (left) Low resolution (right) High resolution TEM image of CdSe-TiO_2 nanostructrures

5.5.3 EDX spectra analysis

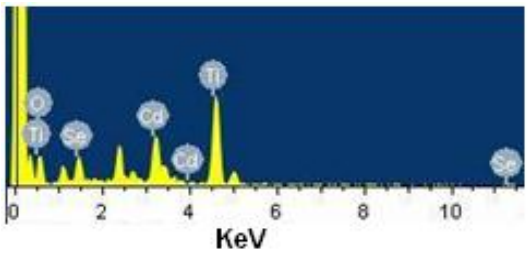

Fig 5.14: EDX spectrum of CdSe-TiO_2 core-shell nanocomposites

The EDX spectrum confirms the presence of all constituent elements i.e Cd, Se, Ti and O in the core-shell CdSe/TiO_2 nanocomposites.

5.6 Optical Property analysis

5.6.1 UV-vis absorbance spectra analysis

Fig 5.15 shows the UV-vis absorbance spectra of both core CdSe and core-shell CdSe-TiO_2 nanoparticles. For both samples, the absorption onset appeared at ~550 nm, blue-shifting 166 nm compared with bulk CdSe (716 nm), which was caused by quantum confinement effect. This indicates that the particle size is very small compared to its bulk counterpart. The absorbance maxima for CdSe occurs at 470 nm which is same

for the core-shell CdSe-TiO_2. It can be seen that the absorbance intensity has increased significantly in the core-shell structure extending to almost infrared regime.

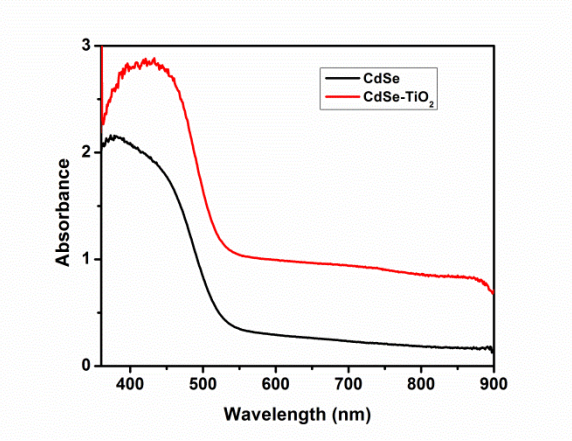

Fig 5.15: UV-vis absorbance spectra of core CdSe and core-shell CdSe-TiO_2 nanocomposites

The band gap of the samples are calculated with the help of Tauc's plot from the absorbance spectra by using the following equation

$$(h\nu\alpha)^2=A(h\nu-E_g)\ldots\ldots\ldots\ldots\ldots\ldots\ldots\ldots(5.5)$$

Where h=Planck's constant, ν=frequency of the incident light, α=Absorption coefficient, A=Proportionality constant, E_g= Band gap. So by plotting *hν* along X-axis and $(h\nu\alpha)^2$ along Y-axis and taking the intercept of the linear section of the graph, the band gaps are calculated.

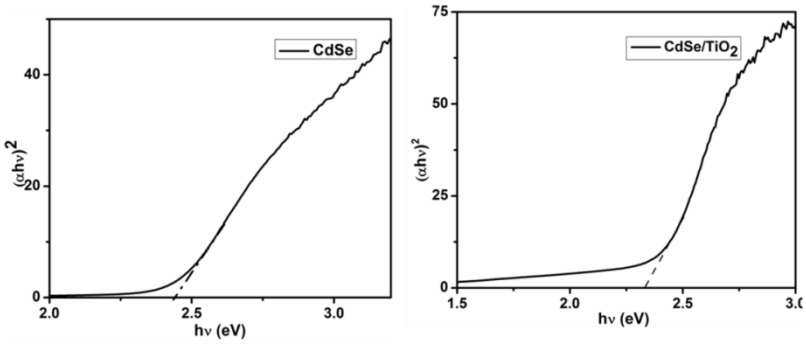

Fig 5.16: Tauc's Plot for (left) CdSe and (right) CdSe-TiO_2

From the fig.5.16, the band gaps are found to be 2.44 eV and 2.33 eV for core CdSe nanoparticles and core-shell CdSe-TiO_2 nanocomposites. It is seen that the band gap is significantly decreased than the bulk band gap 1.7 eV which is another proof of quantum confinement effect that has occurred in the samples. It is also observed that the band gap of the core-shell structure is less than either of the core or of the shell i.e band gap of TiO_2 is 3.2 eV. This gives a hint on the fact that the core-shell structure might be of TYPE 2 which is later confirmed with the help of PL spectra.

Also, for the calculation of Urbach energy, $ln\alpha$ is plotted against E. The reciprocal of the slopes of linear portion, below optical band gap, gives the value of E_μ. The Urbach energy for CdSe and core-shell CdSe-TiO_2 are found to be 1001 meV and 3225 meV respectively. We can see that there is tremendous increase in Urbach energy when CdSe nanoparticles are coated with TiO_2 shell layer. The reason is same like other core-shells we discussed earlier as the growth of the shell results in strain and the formation of defect states at the core/shell interface or within the shell.

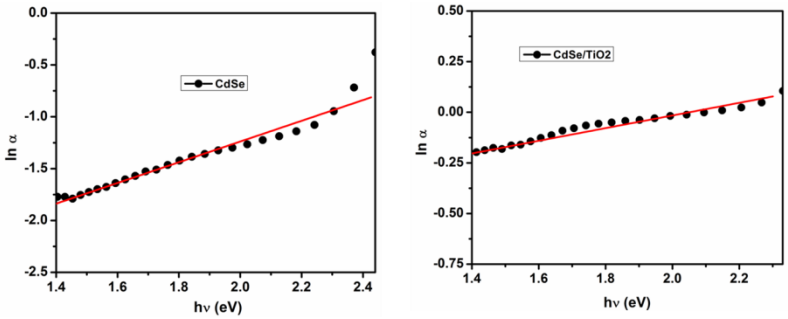

Fig 5.17: Urbach energy plot for (left) CdSe and (right) CdSe-TiO_2

Table 5.5: Calculation of band gap and Urbach energy

Sample name	Urbach energy (meV)	Band gap (eV)
CdSe	1001	2.44
CdSe-TiO_2	3225	2.33

Using the band gap of the nanostructures, we have schematically represented charge separation diagram represented in fig. 5.18.

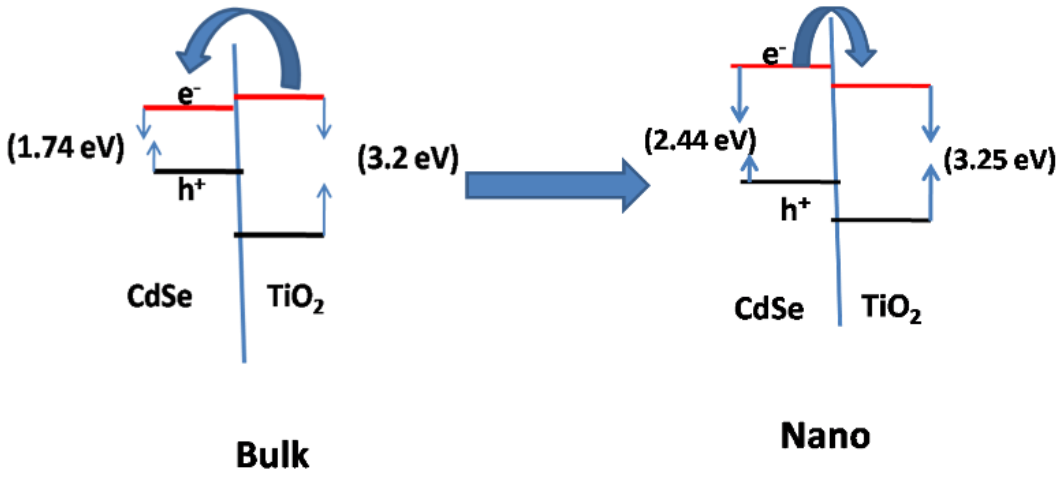

Fig 5.18: Transition from TYPE 1 to TYPE 2 in core-shell CdSe-TiO_2 nanocomposites

Fig. 5.18 shows the band edge alignments in bulk (left) CdSe and TiO_2. It can be clearly seen that the structures form a TYPE 1 heterostructure. But as the size of the core (CdSe) is decreased to nanometer, there is increment in band gap due to size quantization. When the band gap is increased the conduction band moves upward and valence band moves downward. But the shift in conduction band is more prominent than that in valence band. Thus as we can see in the band alignment picture (right) in nanosize core-shell CdSe-TiO_2, it completely attains a TYPE 2 heterostructure which favours charge separation by accommodating the electron in the conduction band of shell TiO_2 and confining the hole in valence band of core CdSe.

5.6.2 Photoluminescence spectra analysis

Fig. 5.19 shows the comparative PL spectra of core CdSe and core-shell CdSe-TiO_2 nanocomposites . We can see that that PL peaks are very broad and shows two distinct peaks at 525 nm and 600 nm for CdSe nanoparticles. The peaks are visibly red shifted in the core-shell structure indicating larger particle size than the core one. The reason for the generation of defect-related emission may be that the extremely small diameter has a very high surface to-volume ratio, and the high-density dangling bonds and trap sites on the surface is easy to be formed and difficult to be passivated. It can be seen that the PL intensity is significantly reduced in the core-shell structure which is due to very less charge recombination in the sample thus confirming the TYPE 2 structure.

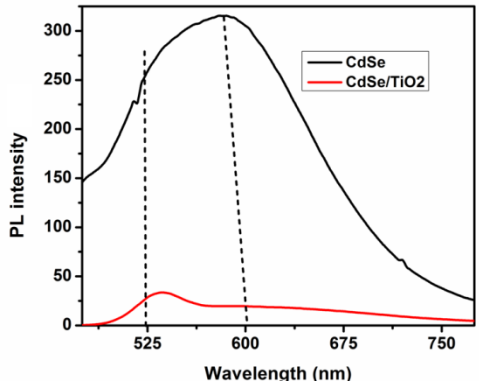

Fig 5.19: Comparative PL diagram for CdSe/TiO_2 core-shell nanocomposite

5.6.3 Photocatalytic activity

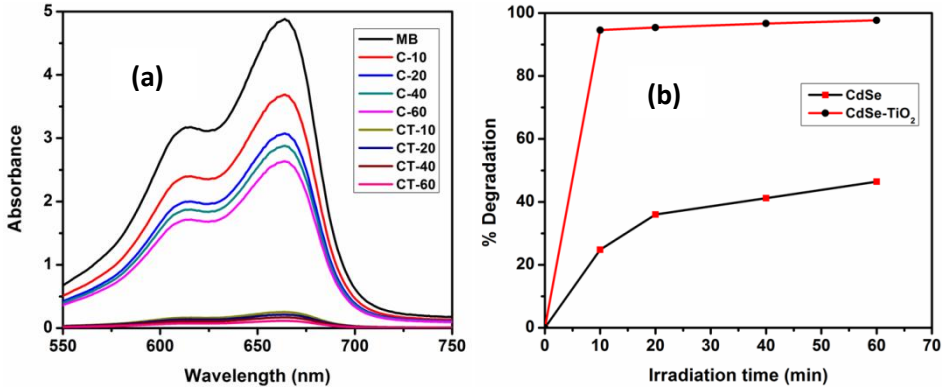

Fig 5.20: (a) Absorbance of methylene blue in presence of catalyst (b) % degradation

Table 5.6: Calculation of % degradation under different illumination time

Sample name	% Degradation w.r.t time of irradiation			
	10 min	20 min	40 min	60 min
CdSe	24.8	36	41.2	46.4
CdSe-TiO_2	94.6	95.4	96.7	97.7

The photocatalytic experiment for both core CdSe and core-shell CdSe-TiO_2 nanostructure were carried out under day light illumination for MB dye. The catalyst and dye amounts were taken in the same procedure as we have described in section 5.3.3. The decrease in concentration or degradation of MB from its initial concentration (C_0) was studied by the decrease in the absorption peak (C_t) of MB

solution irradiated for namely 10, 20, 40 and 60 min. The degradation efficiency of MB solution is given by $\{(A_0-A_t)/A_0\}\times100\%$. From the table it is precisely clear that the degradation efficiency of the core-shell nanostructure is far better than its core counterpart. As it has already been established that for a material to serve as a superior photocatalyst, it should fulfill certain criterions namely (1) Charge generation throughout the whole solar spectrum and (2) charge separation so that free charge carriers are available to take part in the oxidation-reduction reaction for photocatalytic degradation. From UV-vis spectra (fig. 5.15), we can see that the core-shell structure exhibits very high absorbance throughout the whole solar spectrum. Again. The prominent charge separation in core-shell CdSe-TiO_2 nanocomposite is established through fig. 5.18.This is due to the fact that owing to the TYPE 2 nature of the core-shell nanocomposite, the charge separation in the sample is very high which allows free electrons and holes to take part in oxidation and reduction reaction thus leading to enhanced photocatalytic activity. Also as described in chapter 4 (section 4.4), here also charge transfer from conduction band of CdSe to same of TiO_2 occurs which enhances the spatial charge separation reducing the recombination of electron and hole. That is why, we have obtained photocatalytic degradation upto an extent of 97.7% in case of core-shell CdSe-TiO_2 nanocomposites under 60 min daylight illumination for degradation of MB dye.

Conclusion

Thus in this chapter we have investigated the optical as well as photocatalytic properties of two core-shell nanostructure TiO_2-ZrO_2 and CdSe-TiO_2. We also answered the questions with which we started this chapter. We have established from the spectroscopic analysis that both TYPE 1 core-shells are transformed to TYPE 2 due to generation of defect related states and size quantization effect. Further coating of TiO_2 layer over CdSe greatly enhanced the photocatalytic activity by improving the charge separation at the interface of the core-shell nanostructure.

References

[1] Kumari, L., et al. Monoclinic zirconium oxide nanostructures synthesized by a hydrothermal route, *Nanotechnology* **19,** 195602--195609, 2008.

[2] Khanchandani, S., et al. Shell Thickness Dependent Photocatalytic Properties of ZnO/CdS Core−Shell Nanorods, *J. Phys. Chem. C.* **116**, 23653--23666, 2012.

[3] Choudhury, B., & Choudhury, A. Dopant induced changes in structural and optical properties of Cr doped TiO2 nanoparticles, *Mater. Chem. Phys*. **132** (2-3), 1112--1118, 2012.

[4] Brojcin, M.G., et al. Infrared study of laser synthesized anatase TiO_2 nanopowders, *J. Phys. D: Appl. Phys.* **38** (9), 1415--1420, 2005.

[5] Zhang, W.F., et al. Raman scattering study of anatase TiO_2 nanocrystals, *J. Phys. D: Appl. Phys.* **33** (8), 912--916, 2000.

[6] Zhang, J., et al. UV Raman spectroscopic study on TiO_2:I: Phase transformation at the surface and in the bulk , *J. Phys. Chem. B.* **110** (2), 927--935, 2006.

[7] Xu, C.Y., et al. Blue shift of Raman peak from coated TiO_2 nanoparticles, *J. Raman Spectrosc.* **32** (10), 862--865, 2001.

[8] Liu, J., et al. Structure and photoluminescence study of TiO_2 nanoneedle texture along vertically aligned carbon nanofibre arrays, *J. Phys. Chem. C.* **112** (44), 17127--17132, 2008.

[9] Yu, J., et al. Effects of F-doping on the photocatalytic and microstructure of nanocrystalline TiO_2 powders, *Chem. Mater*. **14** (9), 3808--3816, 2002.

[10] Choudhury, B., et al. Extending Photocatalytic Activity of TiO_2 Nanoparticles to Visible Region of Illumination by Doping of Cerium, *Photochemistry and Photobiology* **88,** 257--264, 2012.

[11] Wang, Y., et al., One-Pot Synthesis of CdSe Quantum Dots Using Selenium Dioxide as a Selenium Source in Aqueous Solution, *Bull. Korean Chem*. Soc. **32** (7), 2316--2318, 2011.